



# Non-porous viscous fingering of a thin film of fluid spreading over a lubricated substrate

Haolin Yang<sup>1</sup> and Katarzyna N. Kowal<sup>1</sup> 

<sup>1</sup>School of Mathematics and Statistics, University of Glasgow, Glasgow G12 8QQ, UK

Corresponding author: Katarzyna N. Kowal, [katarzyna.kowal@glasgow.ac.uk](mailto:katarzyna.kowal@glasgow.ac.uk)

(Received 9 December 2024; revised 29 March 2025; accepted 7 May 2025)

Viscous fingering instabilities, common in confined environments such as porous media or Hele-Shaw cells, surprisingly also occur in unconfined, non-porous settings as revealed by recent experiments. These novel instabilities involve free-surface flows of dissimilar viscosity. We demonstrate that such a free-surface flow, involving a thin film of viscous fluid spreading over a substrate that is prewetted with a fluid of higher viscosity, is susceptible to a similar type of novel viscous fingering instability. Such flows are relevant to a range of geophysical, industrial and physiological applications from the small scales of thin-film coating applications and nasal drug delivery to the large scales of lava flows. In developing a theoretical framework, we assume that the intruding layer and the liquid film over which it flows are both long and thin, the effects of inertia and surface tension are negligible, and both layers are driven by gravity and resisted by viscous shear stress so that the principles of lubrication theory hold. We investigate the stability of axisymmetric similarity solutions, describing the base flow, by examining the growth of small-amplitude non-axisymmetric perturbations. We characterise regions of instability across parameter space and find that these instabilities emerge above a critical viscosity ratio. That is, a fluid of low viscosity intruding into another fluid of sufficiently high viscosity is susceptible to instability, akin to traditional viscous fingering in a porous medium. We identify the mechanism of instability, compare with other frontal instabilities and demonstrate that high enough density differences suppress the instability completely.

**Key words:** thin films, fingering instability, gravity currents

## 1. Introduction

Viscous fingering instabilities involve complex, finger-like patterning that emerges when a less viscous fluid invades a more viscous fluid in a porous medium or Hele-Shaw

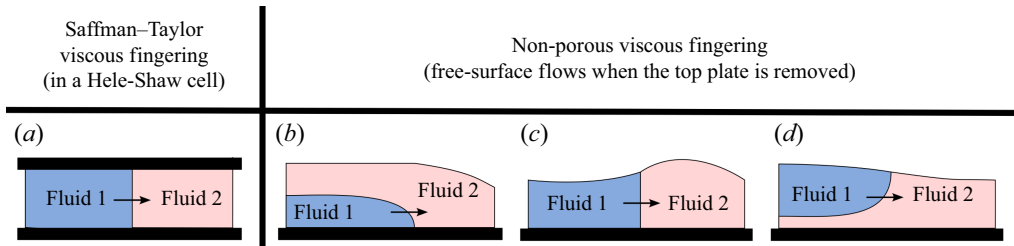


Figure 1. Vertical cross-section of base flows susceptible to (a) classical viscous fingering instabilities (flows in a Hele–Shaw cell or other porous medium) and (b–d) non-porous viscous fingering (free-surface flows). Fluid 1 is less viscous than fluid 2.

cell (Saffman & Taylor 1958; Homsy 1987). What has not been known until recently is that a similar type of viscous fingering instability also occurs in unconfined settings that do not involve porous media or Hele–Shaw cells. In particular, the interaction of the free-surface flows of two fluids of dissimilar viscosity manifests similar instabilities in various configurations depicted in figure 1(b–d). These configurations differ topologically from flows susceptible to classical viscous fingering instabilities, depicted in figure 1(a), through the lack of an upper rigid boundary, which brings with it the need to depart from the use of Darcy’s law for flow in porous media and the need to determine the upper free surface as part of the flow. Efforts to suppress this class of instabilities of free-surface flows while maintaining basal lubrication on the large scale led to the design of a structured substrate – a large-scale analogue of superhydrophobic substrates – which has been shown to give rise to a Navier-type slip macroscopically (Yan & Kowal 2024).

The first examined configuration (figure 1b) of flows susceptible to the novel instability involves the free-surface flow of a thin film of viscous fluid spreading beneath another viscous fluid, as seen in the experiments of Kowal & Worster (2015, 2019a,b) and Kumar *et al.* (2021). Such a flow becomes unstable to a novel cross-flow fingering instability when the intruding fluid is less viscous. Another configuration (figure 1c), leading to similar instabilities, is one in which the intruding fluid fully displaces another viscous fluid (Kowal 2021). The final configuration (figure 1d) is one in which the intruding fluid spreads above a pre-existing thin film of viscous fluid, as seen in the experiments of Dauck (2020), which focused on the limit in which the two layers are of equal density. We examine flows in the final configuration in the present paper, completing the family of flows susceptible to the novel frontal instability.

Such free-surface flows are relevant to a range of phenomena involving the interaction of fluids of different viscosity. An example includes the nasal delivery of drugs and vaccines, which commonly results in what is referred to as nasal dripping in the medical community (Masiuk, Kadakia & Wang 2016). Nasal dripping, or fingering, observed in this context results from the interaction of a low-viscosity drug solution or vaccine with a more viscous mucus. Such fingering is more pronounced the higher the viscosity ratio between the mucus and drug solution or vaccine, as observed in experiments involving synthetic mucus and the drug Avicel (Masiuk *et al.* 2016). Other examples include the interaction between liquid sulphide and silicate melt in a partially solidified (or mostly unsolidified) magmatic system or, more generally, the interaction of lava flows of different viscosity following cooling (Fink & Griffiths 1990, 1998; Balmforth & Craster 2000). Mention has also been made of a link to the flow of ice sheets over less viscous subglacial till, as explored theoretically and experimentally (Kumar *et al.* 2021; Gyllenberg & Sayag 2022).

The new class of instabilities of such free-surface flows have been termed non-porous viscous fingering instabilities, to reflect that they are not associated with porous media

and that the mechanism of instability is similar to that of traditional viscous fingering instabilities, despite the lack of confinement (Kowal 2021). Such instabilities can be thought of as an ultrasoft analogue of fingering in soft/deformable porous media. The latter type of instability is partially suppressed by the elastic deformation of the porous medium or Hele-Shaw cell (Pihler-Puzovic *et al.* 2012, 2013). A simple representation of such a deformable porous medium involves a horizontal Hele-Shaw cell in which its upper wall is replaced by an elastic sheet that is free to deform when a less viscous fluid is injected (Pihler-Puzovic *et al.* 2013, 2013). Such instabilities are increasingly suppressed as the thickness of the sheet decreases. In this work, we remove the elastic sheet completely, falling into the realm of free-surface flows, rather than porous-media flows. Alternatively, we remove the upper wall of a rigid horizontal Hele-Shaw cell depicted in figure 1(a). As a result, Darcy's law no longer applies.

Non-porous viscous fingering instabilities bring similarities to thermoviscous fingering of free-surface flows, in which the viscosity contrast required for onset of instability is driven thermally (Hindmarsh 2004, 2009; Algwaish & Naire 2023). We also find it worthwhile to note the difference between non-porous viscous fingering instabilities and fingering of a driven spreading film (Huppert 1982a; Troian *et al.* 1989). Although both of these involve frontal instabilities of free-surface flows, the former requires a viscosity difference between two fluids and the latter does not, as it involves a single fluid only. The latter instability is, importantly, one in which surface tension is key. As such, non-porous viscous fingering is more closely comparable to viscous fingering in porous media, despite no presence of a porous medium itself.

Viscous fingering in porous media, including Hele-Shaw cells, received considerable attention throughout the last few decades following the seminal work of Saffman & Taylor (1958). This stemmed mainly from its broad range of applications, ranging from enhanced oil recovery (Orr & Taber 1984) to coating applications (Taylor 1963) and carbon sequestration (Cinar, Riaz & Tchelepi 2009). Similar instabilities are also frequently observed in nature, such as in crystal growth (Mullins & Sekerka 1964), the spreading of bacterial colonies (Ben-Jacob 1997), the dynamics of fractures (Hull 1999) and the instability of flame fronts (Ben-Jacob *et al.* 1992).

Interest has since emerged in the ability to either enhance or suppress these instabilities, and to manipulate the patterns that emerge, as desired, for industrial applications. Such control mechanisms have been found to depend upon a number of physical factors, including the injection rate of the less viscous fluid (Li *et al.* 2009; Dias & Miranda 2010), the miscibility of the two fluids involved (Perkins, Johnston & Hoffman 1965) and their rheology (Kondic, Shelley & Palffy-Muhoray 1998; Fast *et al.* 2001). Other effects that enhance or suppress these instabilities include changes in the viscosity ratio of the two fluids (Bischofberger, Ramachandran & Nagel 2014) and introducing particles (Luo, Chen & Lee 2018), for instance. Alterations in the geometry of the porous medium also influence the fingering patterns, when the alterations are both static (Nase, Derks & Lindner 2011; Al-Housseiny, Tsai & Stone 2012) and dynamic (Juel 2012; Zheng, Kim & Stone 2015; Morrow, Moroney & McCue 2019; Vaquero-Stainer *et al.* 2019).

There are a number of similarities between traditional viscous fingering instabilities in porous media and the recently discovered non-porous viscous fingering instabilities. Stability analyses (in the configuration of figure 1b) indicate that the latter instabilities emerge when the jump in hydrostatic pressure gradient across the intrusion front is negative (Kowal & Worster 2019a,b; Kowal 2021). This is similar to, yet contrasts with, traditional viscous fingering instabilities in porous media (figure 1a), which are instead driven by a jump in dynamic pressure gradient (Homsy 1987). Both types of instabilities occur when the intruding viscous fluid is less viscous than the layer into which it intrudes, as has been

seen in experiments in which the injected fluid intrudes from below (Kowal & Worster 2015, 2019a, figure 1b) and from above (Dauck 2020, figure 1d). The latter experiments involved fluids of equal density. However, it has been found that non-zero density differences between the two layers of viscous fluid can suppress these instabilities when the injected fluid intrudes from below (Kowal & Worster 2019b, figure 1b). A similar observation has been found when the fluids are non-Newtonian (Leung & Kowal 2022b, figure 1b).

In this work, we demonstrate similar suppression when the intruding fluid is supplied from above, as depicted in figure 1(d). In particular, we examine the formation of viscous fingering instabilities that emerge when a viscous gravity current intrudes radially outwards over another thin film of viscous fluid, where the two fluids are of unequal densities and viscosities. By conducting a linear stability analysis using the axisymmetric similarity solutions of the companion paper Yang, Mottram & Kowal (2024) as the base flow, we characterise the parameter space over which these instabilities occur. We also compare these instabilities with related fingering instabilities that emerge when the injected fluid intrudes from below. To formulate the problem, we build directly upon the framework of Dauck *et al.* (2019) and Yang *et al.* (2024) by allowing for variations in the azimuthal direction. We also refer to the experiments of Dauck (2020), where similar frontal instabilities emerge. The linear stability analysis of Dauck (2020), focusing on the limit in which the two layers are of equal density, also confirms these instabilities but did not reveal a most unstable wavenumber, much like the equal-density stability calculations of Kowal & Worster (2019b) when the less viscous fluid intrudes from below and growth rates increase with the wavenumber indefinitely. Interestingly, no instabilities were observed in related experiments of Lister & Kerr (1989), involving a thin film of viscous fluid intruding at a fluid interface, save for small-scale frontal patterning attributed to contamination of the fluid surface by dust. We find through our stability calculations that the parameter regime in which the latter experiments were performed corresponds to stable configurations. Other relevant works include single-layer (Smith 1969; Huppert 1982a,b) and two-layer (Kowal & Worster 2015; Dauck *et al.* 2019; Shah, Pegler & Minchew 2021) flows over horizontal and inclined substrates, and non-Newtonian analogues (Hewitt 2013; Gyllenberg & Sayag 2022; Hinton 2022; Christy & Hinton 2023), to name a few.

We begin with a theoretical development in § 2, in which the geometry of the problem, the assumptions and the governing equations are laid out. We investigate the stability of the flow to small non-axisymmetric disturbances by performing a linear stability analysis in § 3, in which we also derive asymptotic solutions for perturbations around a stress singularity at the injection front. We solve the resulting perturbation equations numerically, characterise the instability across parameter space and further discuss our results in § 4. We finalise with concluding remarks in § 5.

## 2. Theoretical development

As depicted in figure 2, we consider the flow of two thin films of incompressible, Newtonian viscous fluids of constant viscosities  $\mu_u$  and  $\mu_l$  and constant densities  $\rho_u$  and  $\rho_l$  in an axisymmetric geometry. The subscripts  $u$  and  $l$  correspond to quantities involving the upper and lower layers, respectively. The subscript  $l$  also describes quantities ahead of the intrusion front. We assume that the effects of inertia and surface tension are negligible and that both fluid layers are long and thin, and are resisted dominantly by vertical shear stresses within the limits of lubrication theory.

We note that the use of the lubrication approximation reflects an idealised scenario in which only vertical shear stress appears, and we aim to determine whether or not this suffices to explain the emergence of instability. Strictly speaking, the approximations of

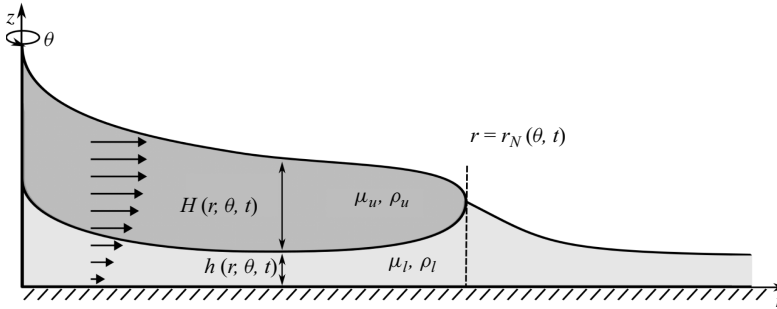


Figure 2. Schematic of a thin film of viscous fluid spreading over a lubricated substrate in an axisymmetric geometry. Schematic adapted from Yang *et al.* (2024).

lubrication theory break down at the nose, where there is a frontal stress singularity, thus warranting the need for the solution of the full Stokes equations near the nose. We do not attempt this in this paper. We note that the experiments of Dauck (2020), performed in a similar configuration to the present paper, and their close agreement to theoretical predictions (which make use of lubrication theory) for their propagation and shape (Dauck *et al.* 2019; Dauck 2020), give credence to the use of lubrication theory at least as a first attempt upon which higher-order corrections can be made in the future. Another similar example is the experiments and stability analysis of Kowal & Worster (2019b), which similarly made use of the lubrication approximation, albeit in a different configuration (in that the less viscous fluid intrudes from below rather than from above).

The two fluids are supplied at constant fluxes  $\hat{Q}_u$  and  $\hat{Q}_l$  at the origin and spread radially outwards over a horizontal, rigid substrate, which is prewetted by the lower-layer fluid to an initial, uniform depth  $h_\infty$ . While the two fluids spread radially outwards, we allow for non-axisymmetric variations in the flow. The upper current extends to the intrusion front  $r = r_N(\theta, t)$ , which splits the domain into two regions: a two-layer region  $0 < r < r_N$ , involving both viscous fluids, and a single-layer region  $r > r_N$ , involving a single viscous fluid of the same material properties as the underlying layer of the two-layer region. The thicknesses of the upper and lower layers are denoted by  $H(r, \theta, t)$  and  $h(r, \theta, t)$ , respectively.

Applying the standard lubrication approximation (see Yang *et al.* (2024) for details of the derivation in the axisymmetric case) results in the following mass conservation equations:

$$\frac{\partial H}{\partial t} + \nabla \cdot \mathbf{q}_u = 0, \quad (2.1)$$

$$\frac{\partial h}{\partial t} + \nabla \cdot \mathbf{q}_l = 0, \quad (2.2)$$

within the two layers, where the depth-integrated fluxes of upper- and lower-layer fluid are given by

$$\mathbf{q}_u = \begin{cases} -\frac{\rho_u g}{3\mu_l} \left[ \left( \mathcal{M}H^3 + \frac{3}{2}Hh^2 + 3H^2h \right) (\nabla H + \nabla h) + \frac{3}{2}\mathcal{D}Hh^2\nabla h \right] & (0 < r < r_N), \\ 0 & (r \geq r_N), \end{cases} \quad (2.3)$$

$$\mathbf{q}_l = \begin{cases} -\frac{\rho_u g}{3\mu_l} \left[ \left( \frac{3}{2}Hh^2 + h^3 \right) (\nabla H + \nabla h) + \mathcal{D}h^3\nabla h \right] & (0 < r < r_N), \\ -\frac{\rho_u g}{3\mu_l} (\mathcal{D} + 1)h^3\nabla h & (r \geq r_N), \end{cases} \quad (2.4)$$

in terms of the dimensionless parameters

$$\mathcal{M} = \frac{\mu_l}{\mu_u} \quad \text{and} \quad \mathcal{D} = \frac{\rho_l - \rho_u}{\rho_u}, \quad (2.5)$$

which denote the viscosity ratio and relative density difference, respectively. In general, the quantities described here may vary in  $\theta$ . Here,  $g$  refers to the gravitational acceleration.

At the origin,  $r = 0$ , we assume that the upper and lower layers are supplied at a constant flux  $\hat{Q}_l$ ,  $\hat{Q}_u$ , respectively, so that

$$\lim_{r \rightarrow 0} 2\pi r \mathbf{q}_u \cdot \mathbf{e}_r = \hat{Q}_u, \quad (2.6)$$

$$\lim_{r \rightarrow 0} 2\pi r \mathbf{q}_l \cdot \mathbf{e}_r = \hat{Q}_l, \quad (2.7)$$

where  $\mathbf{e}_r$  is the radial unit basis vector.

The thickness and the normal flux of the lower layer are continuous across the intrusion front  $r = r_N(\theta, t)$ , so that

$$[h]_-^+ = 0 \quad \text{at } r = r_N, \quad (2.8)$$

$$[\mathbf{q}_l \cdot \mathbf{n}]_-^+ = 0 \quad \text{at } r = r_N, \quad (2.9)$$

where  $\mathbf{n}$  is the outward unit normal vector to the intrusion front. In addition, the normal component of the upper-layer flux vanishes at the front, so that

$$\mathbf{q}_u \cdot \mathbf{n} = 0 \quad \text{at } r = r_N. \quad (2.10)$$

The front evolves kinematically, so that

$$\dot{r}_N = \lim_{r \rightarrow r_N^-} H^{-1} \mathbf{q}_u \cdot \nabla(r - r_N) = \lim_{r \rightarrow r_N^-} \left[ \frac{\mathbf{q}_u \cdot \mathbf{e}_r}{H} - \frac{\mathbf{q}_u \cdot \mathbf{e}_\theta}{H r_N} \frac{\partial r_N}{\partial \theta} \right]. \quad (2.11)$$

Here,  $\mathbf{e}_\theta$  is the azimuthal unit basis vector. In the far field, we assume that the thickness is uniform so that

$$\lim_{r \rightarrow \infty} h = h_\infty. \quad (2.12)$$

These governing equations, boundary conditions, matching conditions, and the evolution equation for the front fully specify the moving boundary problem considered in this paper.

### 3. Non-axisymmetric disturbances

We investigate the evolution of non-axisymmetric disturbances of the base flow by expanding about the zeroth-order axisymmetric similarity solutions of Yang *et al.* (2024). To do so, we change the independent variables  $(r, \theta, t)$  to  $(\xi, \vartheta, \tau)$  and non-dimensionalise the system by applying the following transformations

$$(\xi, \xi_N(\vartheta, \tau)) = \left( \frac{3\mu_l}{\rho_u g h_\infty^3 t} \right)^{1/2} (r, r_N(\theta, t)), \quad \vartheta = \theta, \quad \tau = \log(t/t_0), \quad (3.1)$$

$$(F(\xi, \vartheta, \tau), f(\xi, \vartheta, \tau)) = h_\infty^{-1} (H(r, \theta, t), h(r, \theta, t)), \quad (3.2)$$

$$(\phi_u(\xi, \vartheta, \tau), \phi_l(\xi, \vartheta, \tau)) = \left( \frac{3\mu_l t}{\rho_u g h_\infty^5} \right)^{1/2} (\mathbf{q}_u(r, \theta, t), \mathbf{q}_l(r, \theta, t)), \quad (3.3)$$

where  $t_0 = 3\mu_l/(\rho_u g h_\infty)$ . We also rescale the two input source fluxes at the origin so that

$$\mathcal{Q}_u = \hat{Q}_u/\hat{Q} \quad \text{and} \quad \mathcal{Q}_l = \hat{Q}_l/\hat{Q}, \quad (3.4)$$



where

$$\hat{Q} = 2\pi h_{\infty}^4 \frac{\rho_u g}{3\mu_l} \quad (3.5)$$

is a dimensional measure of the lower-layer flux associated with a depth of  $h_{\infty}$ . Alternatively, the parameter  $\hat{Q}$  can be interpreted as the flux required to attain a thickness of  $h_{\infty}$  near the source.

The transformation (3.1)–(3.3) into similarity space transforms the base flow (the similarity solutions of Yang *et al.* (2024)) into a steady solution, which is key to allow a straightforward stability analysis to be performed. This can be seen by examining the transformed system of partial differential equations

$$\frac{\partial F}{\partial \tau} - \frac{1}{2} \frac{\partial F}{\partial \xi} \xi + \frac{1}{\xi} \frac{\partial (\xi \phi_{ur})}{\partial \xi} + \frac{1}{\xi} \frac{\partial \phi_{u\theta}}{\partial \vartheta} = 0, \quad (3.6)$$

$$\frac{\partial f}{\partial \tau} - \frac{1}{2} \frac{\partial f}{\partial \xi} \xi + \frac{1}{\xi} \frac{\partial (\xi \phi_{lr})}{\partial \xi} + \frac{1}{\xi} \frac{\partial \phi_{l\theta}}{\partial \vartheta} = 0, \quad (3.7)$$

describing mass conservation within the two layers of viscous fluid, the coefficients of which are independent of the transformed time variable  $\tau$ . Here, the radial and azimuthal components of the depth-integrated fluxes of the two layers of fluid are given by

$$(\phi_{ur}, \phi_{lr}) = (\boldsymbol{\phi}_u \cdot \mathbf{e}_r, \boldsymbol{\phi}_l \cdot \mathbf{e}_r), \quad (3.8)$$

$$(\phi_{u\theta}, \phi_{l\theta}) = (\boldsymbol{\phi}_u \cdot \mathbf{e}_{\theta}, \boldsymbol{\phi}_l \cdot \mathbf{e}_{\theta}), \quad (3.9)$$

where

$$\boldsymbol{\phi}_u = \begin{cases} - \left[ \left( \mathcal{M}F^3 + \frac{3}{2}Ff^2 + 3F^2f \right) (\nabla F + \nabla f) + \frac{3}{2}\mathcal{D}Ff^2\nabla f \right] & (0 < \xi < \xi_N) \\ 0 & (\xi \geq \xi_N), \end{cases} \quad (3.10)$$

$$\boldsymbol{\phi}_l = \begin{cases} - \left[ \left( \frac{3}{2}Ff^2 + f^3 \right) (\nabla F + \nabla f) + \mathcal{D}f^3\nabla f \right] & (0 < \xi < \xi_N) \\ -(\mathcal{D} + 1)f^3\nabla f & (\xi \geq \xi_N), \end{cases} \quad (3.11)$$

for the upper and lower layers, respectively. The operator  $\nabla$  is now the gradient operator in the two-dimensional polar coordinate system spanned by  $(\xi, \vartheta)$ .

As for the boundary conditions, the source flux boundary conditions reduce to

$$\xi \phi_{ur} \rightarrow \mathcal{Q}_u, \quad \xi \phi_{lr} \rightarrow \mathcal{Q}_l \quad (\xi \rightarrow 0), \quad (3.12)$$

while the matching conditions at the intrusion front, describing continuity of lower-layer thickness, continuity of lower-layer flux and the zero-flux condition for the upper layer, are given by

$$[f]_{-}^{+} = 0, \quad [\boldsymbol{\phi}_l \cdot \mathbf{n}]_{-}^{+} = 0, \quad \boldsymbol{\phi}_u \cdot \mathbf{n} = 0 \quad (\xi = \xi_N), \quad (3.13)$$

respectively, where the normal vector at the intrusion front becomes

$$\mathbf{n} = \left( \mathbf{e}_r - \frac{1}{\xi_N} \frac{\partial \xi_N}{\partial \vartheta} \mathbf{e}_{\theta} \right) \left( 1 + \left( \frac{1}{\xi_N} \frac{\partial \xi_N}{\partial \vartheta} \right)^2 \right)^{-1/2}. \quad (3.14)$$

These are supplemented by the kinematic condition, which reduces to

$$\frac{\mathbf{e}_r \cdot \boldsymbol{\phi}_u}{F} - \frac{1}{\xi_N} \frac{\partial \xi_N}{\partial \vartheta} \frac{\mathbf{e}_{\theta} \cdot \boldsymbol{\phi}_u}{F} \rightarrow \frac{\partial \xi_N}{\partial \tau} + \frac{1}{2} \xi_N \quad (\xi \rightarrow \xi_N^{-}), \quad (3.15)$$

and the far-field condition,

$$f \rightarrow 1 \quad (\xi \rightarrow \infty), \quad (3.16)$$

reflecting the choice to scale vertical lengths with respect to the dimensional far-field thickness.

These governing equations are a set of nonlinear partial differential equations describing the flow of general disturbances to the axisymmetric base flow. In a later section, we will focus on small-amplitude disturbances and linearise these equations about the base flow. However, the singular structure of the intrusion front raises problems with formulating the small-amplitude equations and boundary conditions consistently. To avoid these issues, we first investigate the structure of the singularity at the intrusion front in the following section, and then use it to make an informed coordinate transformation that will allow for a consistent set of small-amplitude equations and boundary conditions to be formulated.

### 3.1. Frontal singularity and asymptotic solution

Similar to the behaviour of the unperturbed, axisymmetric flow (the basic state considered in Yang *et al.* (2024)), there is a frontal singularity inherent to the perturbed flow. We generalise the asymptotic analysis of Yang *et al.* (2024) for the unperturbed flow near the intrusion front to include variations in the azimuthal direction and find a generalised asymptotic solution near the front of the form

$$\begin{aligned} F(\xi, \vartheta, \tau) &\sim A_1(\vartheta, \tau) \left(1 - \frac{\xi}{\xi_N}\right)^{\frac{1}{2}} + A_2(\vartheta, \tau) \left(1 - \frac{\xi}{\xi_N}\right) + \dots, \\ f(\xi, \vartheta, \tau) &\sim a_0(\vartheta, \tau) + a_1(\vartheta, \tau) \left(1 - \frac{\xi}{\xi_N}\right)^{\frac{1}{2}} + a_2(\vartheta, \tau) \left(1 - \frac{\xi}{\xi_N}\right) + \dots \end{aligned} \quad (3.17)$$

reflecting a square-root singularity, in contrast to the cube-root frontal singularity of a single-layer viscous gravity current (Huppert 1982b). Here, the relationships between the coefficients  $a_0$ ,  $a_1$ ,  $a_2$ ,  $A_1$  and  $A_2$  are given by

$$a_1 = -\frac{A_1}{\mathcal{D} + 1}, \quad (3.18)$$

$$A_2 = -\frac{4A_1^2}{9a_0} \left( \mathcal{M} - \frac{3}{\mathcal{D} + 1} \right), \quad (3.19)$$

$$a_2 = \frac{1}{9(\mathcal{D} + 1)a_0^2} \left[ 3\xi_N \left( \xi_N + 2\frac{\partial \xi_N}{\partial \tau} \right) + A_1^2 a_0 \left( 4\mathcal{M} - 9 - \frac{3}{\mathcal{D} + 1} \right) \right]. \quad (3.20)$$

As the base flow involves a singularity at the intrusion front, singular terms appear also in the equations governing the perturbations. This prevents one from formulating consistent linearised boundary conditions at the front. A similar problem occurs when linearising about the Barenblatt–Pattle similarity solution and various methods have been introduced to handle it, including the use of the method of strained coordinates (Grundy & McLaughlin 1982) and a transformation of the dependent variable (Mathunjwa & Hogg 2006). Instead, we follow an approach similar to that of Kowal & Worster (2019b) by simply mapping the two-layer region to a fixed interval  $[0, 1]$  via the coordinate transformation

$$\Lambda = \xi/\xi_N. \quad (3.21)$$

Such a coordinate transformation eliminates the need to perturb the position of the singular point, which is now fixed at  $\Lambda = 1$ , for the corresponding boundary conditions. We summarise the equations and boundary conditions for the small-amplitude perturbations



in terms of  $\Lambda$  in the following section. However, to aid numerical integration, we further transform the independent variable nonlinearly by defining

$$\hat{\Lambda} = 1 - (1 - \Lambda)^{1/2} \quad (3.22)$$

in the two-layer region and  $\hat{\Lambda} = \Lambda$  in the single-layer region. The transformation (3.22) is motivated by our asymptotic solution (3.17), which identifies a square-root singularity near the front. Under the transformation (3.22), the thicknesses of the two layers are instead linear near the intrusion front, and hence their gradients no longer diverge. In essence, the frontal singularity is now a removable singularity, which is simpler to handle numerically.

### 3.2. Small-amplitude perturbations

We wish to examine the evolution of small perturbations to the base, axisymmetric flow, and in order to do so, we linearise the transformed problem by defining

$$X(\xi, \vartheta, \tau) \equiv X(\Lambda, \Theta, \mathcal{T}) = X_0(\Lambda) + \epsilon \tilde{X}_1(\Lambda, \Theta, \mathcal{T}) + \dots \quad (3.23)$$

for variables  $X = f, F, \phi_{ur}, \phi_{u\theta}, \phi_{lr}, \phi_{l\theta}, \phi_l, \phi_u$ , where  $\epsilon$  is an arbitrary small number,  $\Theta = \vartheta, \mathcal{T} = \tau$  and

$$\chi = \chi_0 + \epsilon \tilde{\chi}_1(\Theta, \mathcal{T}) + \dots \quad (3.24)$$

for variables  $\chi = \xi_N, a_0, a_1, a_2, A_1, A_2, \mathbf{n}$ . We note that the governing equations and boundary conditions describing the evolution of the basic state (involving variables with the subscript  $_0$ ) are outlined in Yang *et al.* (2024), which we do not repeat here, for brevity.

To examine the evolution of the perturbations, we search for normal mode solutions of the form

$$\tilde{X}_1(\Lambda, \Theta, \mathcal{T}) = X_1(\Lambda) e^{\sigma \mathcal{T} + ik\Theta}, \quad (3.25)$$

$$\tilde{\chi}_1(\Theta, \mathcal{T}) = \chi_1 e^{\sigma \mathcal{T} + ik\Theta}, \quad (3.26)$$

where  $\sigma$  is the growth rate of the perturbations and  $k$  is the azimuthal wavenumber. As the transformed time variable  $\mathcal{T}$  is logarithmic in the sense  $\mathcal{T} = \tau = \log(t/t_0)$ , these normal modes in fact represent algebraic growth/decay of perturbations in physical time  $t$ , since  $e^{\sigma \mathcal{T}}$  is proportional to  $t^\sigma$ . We also note that owing to the transformation  $r_N \propto \xi_N t^{1/2}$ , if the growth rate satisfies  $-1/2 < \sigma < 0$  then the perturbations to  $r_N$  will appear to grow even though the perturbations to  $\xi_N$  decay.

Substitution into (3.6)–(3.16) yields the following expressions for the perturbed fluxes:

$$\phi_{ur1} = \alpha_{u1} f_1 + \alpha_{u2} F_1 + \alpha_{u3} f'_1 + \alpha_{u4} F'_1 + \alpha_{u5} \xi_{N1}, \quad (3.27)$$

$$\phi_{lr1} = \alpha_{l1} f_1 + \alpha_{l2} F_1 + \alpha_{l3} f'_1 + \alpha_{l4} F'_1 + \alpha_{l5} \xi_{N1}, \quad (3.28)$$

$$\phi_{u\theta1} = ik(\alpha_{u3} \Lambda^{-1} f_1 + \alpha_{u4} \Lambda^{-1} F_1 + \alpha_{u5} \xi_{N1}), \quad (3.29)$$

$$\phi_{l\theta1} = ik(\alpha_{l3} \Lambda^{-1} f_1 + \alpha_{l4} \Lambda^{-1} F_1 + \alpha_{l5} \xi_{N1}), \quad (3.30)$$

and the following perturbed governing equations

$$\sigma \left( F_1 - \frac{\xi_{N1}}{\xi_{N0}} \Lambda F'_0 \right) - \frac{1}{2} \Lambda F'_1 - \frac{\xi_{N1}}{\xi_{N0}^2 \Lambda} (\Lambda \phi_{u0})' + \frac{1}{\xi_{N0} \Lambda} (\Lambda \phi_{u1})' + \frac{ik}{\xi_{N0} \Lambda} \phi_{u\theta1} = 0, \quad (3.31)$$

$$\sigma \left( f_1 - \frac{\xi_{N1}}{\xi_{N0}} \Lambda f'_0 \right) - \frac{1}{2} \Lambda f'_1 - \frac{\xi_{N1}}{\xi_{N0}^2 \Lambda} (\Lambda \phi_{l0})' + \frac{1}{\xi_{N0} \Lambda} (\Lambda \phi_{l1})' + \frac{ik}{\xi_{N0} \Lambda} \phi_{l\theta1} = 0, \quad (3.32)$$

reflecting mass conservation within the two layers, where the prime symbol represents the derivative respect to  $\Lambda$  and  $\alpha_{ij}$  are functions of the basic state quantities, including  $f_0$ ,  $F_0$ ,  $f'_0$  and  $F'_0$ , as well as the parameters  $\mathcal{M}$  and  $\mathcal{D}$  and the unperturbed frontal position  $\xi_{N0}$ , as given explicitly in [Appendix B](#).

As for the boundary conditions for the perturbed system, note that the coordinate transformation (3.21) eliminates the need to perturb the value of  $\Lambda$  at which the boundary conditions are applied. The perturbations to the frontal position are instead embedded into the governing equations, and through the appearance of additional terms in some boundary conditions following the linearisation of the normal vector. In particular, we have

$$\Lambda(\xi_{N1}\phi_{ur0} + \xi_{N0}\phi_{ur1}) \rightarrow 0, \quad \Lambda(\xi_{N1}\phi_{lr0} + \xi_{N0}\phi_{lr1}) \rightarrow 0 \quad (\Lambda \rightarrow 0), \quad (3.33)$$

reflecting that both fluids are supplied at a constant flux at the origin, and so the perturbed source fluxes vanish as we approach the origin. The frontal matching conditions for the perturbations reduce to

$$[f_1]^\pm = 0, \quad [\phi_{lr1}]^\pm = 0, \quad \phi_{ur1} = 0 \quad (\Lambda = 1), \quad (3.34)$$

reflecting the fact that the perturbed lower-layer thickness and flux is continuous and the perturbed upper-layer flux vanishes at the intrusion front. In simplifying these conditions, we use that  $\mathbf{n}_0 = \mathbf{e}_r$  and that  $\mathbf{n}_1$  is proportional to the azimuthal basis vector while the flux (for the base flow) is proportional to the radial basis vector, so that  $\phi_{u0} \cdot \mathbf{n}_1 = 0$  and  $\phi_{l0} \cdot \mathbf{n}_1 = 0$ . A linearisation of the kinematic condition yields the following boundary condition for the perturbations:

$$\frac{\phi_{ur1}}{F_0} - \frac{F_1\phi_{ur0}}{F_0^2} \rightarrow \left(\sigma + \frac{1}{2}\right)\xi_{N1} \quad (\Lambda \rightarrow 1^-), \quad (3.35)$$

while the far-field condition requires that the perturbations vanish in the far field,

$$f_1 \rightarrow 0 \quad (\Lambda \rightarrow \infty). \quad (3.36)$$

We note that this is a differential eigenvalue problem, with eigenfunctions  $(X_1, \chi_1)$  and eigenvalues  $\sigma$ . That is, the growth rates  $\sigma$  can be found numerically for each wavenumber  $k$ , which we discuss in the following section.

### 3.3. Numerical method

We solve the perturbation equations in the variable  $\hat{\Lambda}$ , as defined in (3.22), by shooting backwards for  $\xi_{N1}$  and  $Q_{l1}|_{\hat{\Lambda}=L}$  from the far field at  $\hat{\Lambda} = L$ , where we define  $Q_{i1} = \Lambda\phi_{ir}$  for  $i = l, u$  and  $L > 1$  is a constant that is sufficiently large that  $\hat{\Lambda} = L$  acts as a pseudo infinity. To initiate the computations for the single-layer region, we start by specifying values of  $\xi_{N1}$  and  $Q_{l1}|_{\hat{\Lambda}=L}$  and integrating the equations backwards from  $\hat{\Lambda} = L$  towards the intrusion front  $\hat{\Lambda} = 1$ . Because the intrusion front is a singular point for the governing equations of the two-layer region, we use the asymptotic solutions as matching conditions for our numerical solutions. That is, we calculate the asymptotic solution at  $\hat{\Lambda} = 1 - \delta$  using the computed numerical solution of the single-layer region at  $\hat{\Lambda} = 1$ , where  $\delta \ll 1$ . We integrate the perturbation equations for the two-layer region numerically, backwards from  $\hat{\Lambda} = 1 - \delta$  towards  $\hat{\Lambda} = \Delta$ , where  $\Delta \ll 1$ .

By performing an asymptotic analysis for a single-layer viscous gravity current, we find that the general solution for the perturbed dependent variables is of the form

$$X_1 \sim (c_1\hat{\Lambda}^{-k} + c_2\hat{\Lambda}^k)w(\hat{\Lambda}) \quad (3.37)$$

as  $\hat{\Lambda} \rightarrow 0$ , where  $w$  is a function that is at most logarithmically singular at the origin and  $c_1$  and  $c_2$  are arbitrary constants. This reflects a singularity at the origin, which is strongest for large wavenumbers  $k$ . For the purpose of resolving this singularity for all  $k$  in our computations, we use the transformation

$$X_1(\hat{\Lambda}) \equiv \frac{1}{x} \bar{X}_1(x), \quad (3.38)$$

where  $x = \hat{\Lambda}^k$ , within the two-layer region, and solve for  $\bar{X}_1$  numerically as a function of  $x$ .

As the problem is  $2\pi$ -periodic in the azimuthal direction, only integer values of  $k$  are permitted. However, we interpolate for intermediate values of  $k$  for illustrative purposes in displaying the results.

Given a value of the wavenumber  $k$ , the system admits non-zero solutions for specific growth rates, or eigenvalues,  $\sigma$ . To find such solutions, we designed an algorithm by exploiting the linearity of the governing equations and boundary conditions. In particular, for a given wavenumber and set of parameter values, we set a guess for the growth rate and shoot backwards as described earlier. In doing so, we obtain two test solutions, denoted by  $s_1$  and  $s_2$ , where  $s_1$  is calculated by setting  $\xi_{N1} = 1$  and  $Q_{l1}|_{\hat{\Lambda}=L} = 0$  and  $s_2$  is calculated by setting  $\xi_{N1} = 0$  and  $Q_{l1}|_{\hat{\Lambda}=L} = 1$ . These two solutions are linearly independent and satisfy the perturbation equations and boundary conditions except for perhaps the source flux conditions at the origin. Owing to the linearity of the system, any linear combination of the two solutions is also a solution.

In order to quantify the departure from the source flux boundary conditions, we define a residual matrix:

$$\mathbf{R} = \begin{bmatrix} Q_{l1,1} & Q_{l1,2} \\ Q_{u1,1} & Q_{u1,2} \end{bmatrix}, \quad (3.39)$$

where the  $i$ th column measures the perturbed source flux at the origin corresponding to the solution  $s_i$  and  $i = 1, 2$ . If the initial guess for the value of the growth rate  $\sigma$  is correct, it is possible to obtain a linear combination of the two test solutions such that the source flux conditions at the origin are satisfied, i.e.  $Q_{l1} = 0$  and  $Q_{u1} = 0$ . This is equivalent to  $\det(\mathbf{R}) = 0$ , and this particular linear combination is the desired solution to the perturbation equations and all boundary conditions, including the zero source flux boundary conditions. However, if the guessed value of the growth rate is incorrect, then  $\det(\mathbf{R}) \neq 0$ . That is, the growth rate is an admissible eigenvalue if and only if  $\det(\mathbf{R}) = 0$ . We, therefore, wish to find values of the growth rate  $\sigma$  for which  $\det(\mathbf{R}) = 0$  to within a specified tolerance. In essence, this reduces to a one-dimensional root finding problem for  $\sigma$ .

We note that in order to assess stability, it suffices to consider the eigensolution that corresponds to the largest growth rate, as this gives rise to the most unstable mode. We make sure that our computed solutions for  $\sigma$  are largest by manual inspection of plots of the determinant of  $\mathbf{R}$  against the growth rate for a range of test cases. We discuss results, obtained via numerical continuation, in the following section.

#### 4. Discussion

In this section, we discuss the onset of instability and relevant characteristics in terms of the growth rates, interval of unstable wavenumbers and the critical wavenumber and how these vary across parameter space. In particular, we map out the behaviour of small

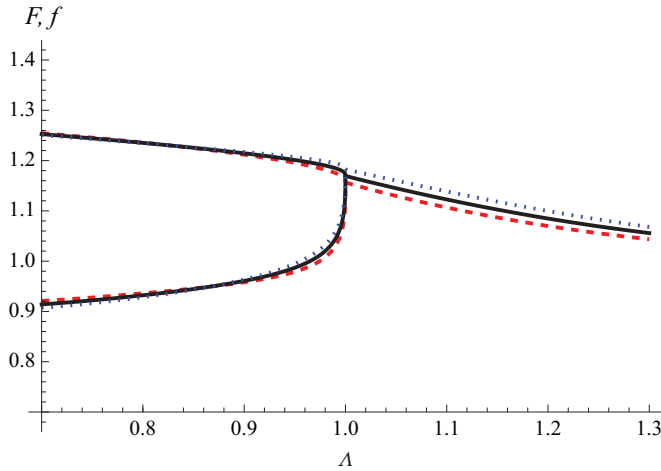


Figure 3. The unperturbed (solid) and perturbed (dashed and dotted) spatial profiles showing the shape of the nose when  $k = 12$ ,  $\mathcal{M} = 200$ ,  $\mathcal{D} = 0.1$ ,  $\mathcal{Q}_u = 1$  and  $\mathcal{Q}_l = 0.2$ . The perturbed profile shown as a dashed (dotted) curve corresponds to intrusions ahead of (behind) the nose of the base flow.

disturbances to the base flow in terms of four key dimensionless quantities: the viscosity ratio  $\mathcal{M}$ , the density difference  $\mathcal{D}$ , the total source flux  $\mathcal{Q}_u + \mathcal{Q}_l$  and the flux ratio  $\mathcal{Q}_l / \mathcal{Q}_u$ .

The spatial structure of the perturbation in an unstable configuration is depicted in figure 3 in comparison with the unperturbed base flow. When the intruding layer is perturbed forwards (backwards), it thickens (thins) and protrudes downwards into (recedes upwards from) the lower layer and the lower layer thins (thickens) near the nose. As discussed further in § 4.2, finger growth requires sufficient protrusion of an intruding less viscous fluid downwards into the more viscous underlying layer, rather than upwards into the less viscous air.

#### 4.1. Thresholds of instability across parameter space

We find that the flow is unstable only for sufficiently large values of the viscosity ratio  $\mathcal{M}$ . That is, the intruding layer of viscous fluid needs to be of sufficiently small viscosity for the flow to become unstable. This criterion is similar to what is necessary for the onset of Saffman–Taylor instabilities in porous media, which occur only when the viscosity of the intruding fluid is lower than that of the ambient fluid (Saffman & Taylor 1958). Sufficiently large viscosity ratios are also necessary for the onset of fingering instabilities when the less viscous fluid intrudes from below a more viscous gravity current (Kowal & Worster 2019a,b; Leung & Kowal 2022a,b), and when it displaces the more viscous current completely (Kowal 2021). Illustrative values of the viscosity ratio necessary for the onset of instability when the less viscous fluid intrudes from above a more viscous gravity current, as examined in this work, can be seen in figure 4. In particular, figure 4 displays the dispersion relation for the growth rate  $\sigma$  as a function of the wavenumber  $k$ , for illustrative parameter values and various values of the viscosity ratio  $\mathcal{M}$ . The growth rate is positive for a bounded interval of wavenumbers only when the viscosity ratio is large enough. That is, the flow is unstable for a bounded interval of wavenumbers only above a critical viscosity ratio. The interval of unstable wavenumbers is shown in figure 5 as a function of the viscosity ratio  $\mathcal{M}$ , where it can be seen that the interval of unstable wavenumbers expands as the viscosity ratio increases. The boundary between the stable and unstable regions, shown in figure 5, depicts the neutral viscosity ratio, defined as the

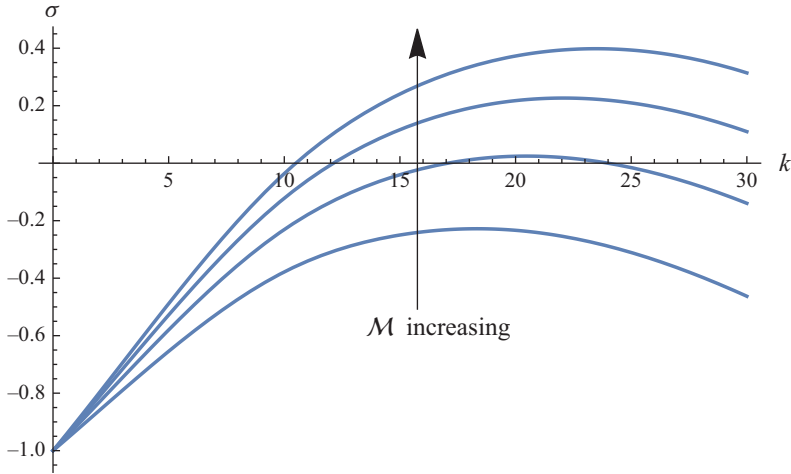


Figure 4. The growth rate versus the wavenumber for various viscosity ratios  $\mathcal{M} = 20, 30, 40, 50$  when  $\mathcal{D} = 0.05$ ,  $\mathcal{Q}_u = 1$ ,  $\mathcal{Q}_l = 1$ .

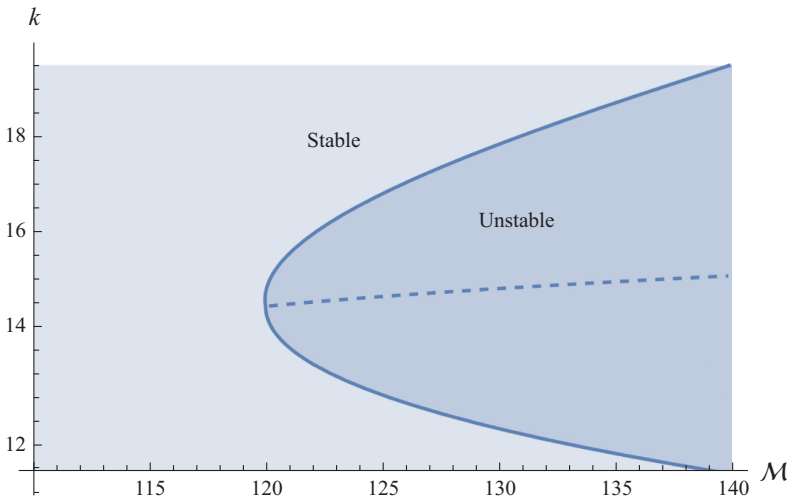


Figure 5. Neutral stability curve (solid) displaying the interval of unstable wavenumbers as a function of the viscosity ratio, also showing the critical wavenumber  $k_c$  (dashed), when  $\mathcal{D} = 0.1$ ,  $\mathcal{Q}_u = 1$  and  $\mathcal{Q}_l = 1$ . The flow is unstable (stable) for large (small) viscosity ratios.

value of the viscosity for which the growth rate is zero. The flow is unstable when the viscosity ratio is above the neutral viscosity ratio. The critical wavenumber  $k_c$ , defined as the wavenumber for which the growth rate is maximal, gradually increases with the wavenumber as depicted in figure 5.

We find that the instability is most profound for low values of the density difference and that it is suppressed completely when the density difference is sufficiently large. This is illustrated in figure 6, depicting an interval of wavenumbers for which the system is unstable below a critical value of the density difference. This interval expands and the critical wavenumber  $k_c$  increases as the density difference decreases, as shown in figure 6. Figure 6 also illustrates that the instability is suppressed completely above a critical value of the density difference. This agrees with stability analyses of flows of thin films of

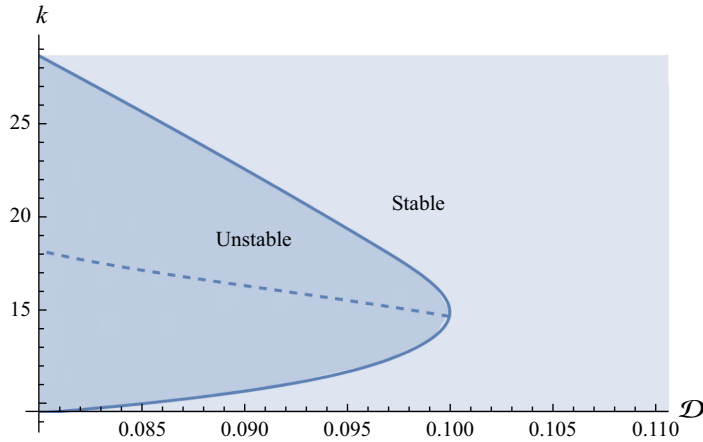


Figure 6. Neutral stability curve (solid) displaying the interval of unstable wavenumbers as a function of the density difference, also showing the critical wavenumber  $k_c$  (dashed), when  $\mathcal{M} = 120$ ,  $\mathcal{Q}_u = 1$  and  $\mathcal{Q}_l = 1$ . The flow is unstable (stable) for small (large) density differences.

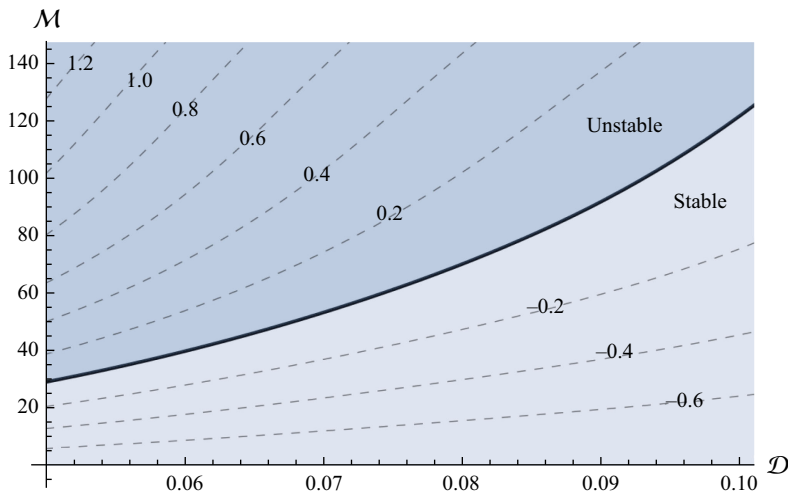


Figure 7. Contour plot of the maximal growth rate  $\sigma_{max}$  versus the viscosity ratio  $\mathcal{M}$  and density difference  $\mathcal{D}$ , with the neutral stability curve ( $\sigma_{max} = 0$ ) displayed as a thick solid curve. The remaining parameter values are  $\mathcal{Q}_u = 1$  and  $\mathcal{Q}_l = 1$ . The flow is unstable for high-viscosity ratios and low-density differences.

viscous fluid intruding underneath another viscous fluid of various rheologies (Kowal & Worster 2019b; Leung & Kowal 2022b).

We condense information in the  $(\mathcal{M}, \mathcal{D})$ -parameter space further in a contour plot of the maximal growth rate  $\sigma_{max}$  versus the viscosity ratio and density difference, depicted in figure 7. Maximal growth rates are largest for large viscosity ratios and small density differences, with viscosity ratios of the order of 10 required for the onset of instability when the density difference is small. This contrasts with instabilities formed when a free-surface flow is penetrated from below by a less viscous fluid (Kowal & Worster 2019a,b) and with classical Saffman–Taylor instabilities in a Hele–Shaw cell (Saffman & Taylor 1958), for which the threshold of instability is of order unity in the viscosity ratio. We discuss why this is to be expected on physical grounds in § 4.2.



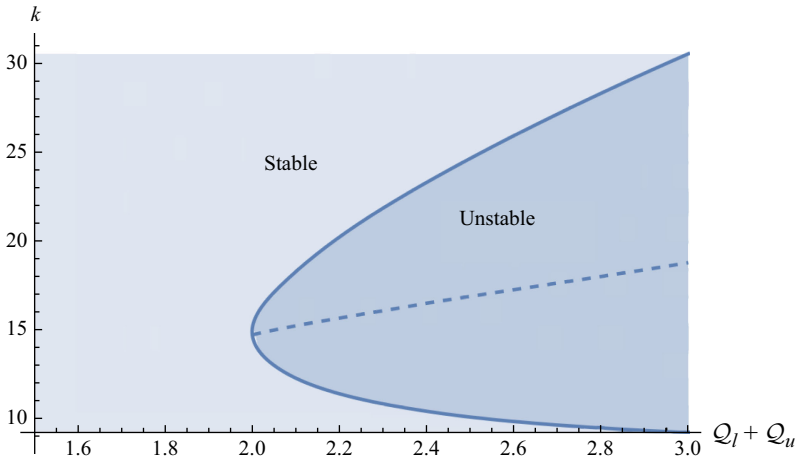


Figure 8. Neutral stability curve (solid) displaying the interval of unstable wavenumbers as a function of the total source flux, also showing the critical wavenumber  $k_c$  (dashed), when  $\mathcal{D} = 0.1$ ,  $\mathcal{M} = 120$  and  $Q_l/Q_u = 1$ . The flow is unstable (stable) for large (small) source fluxes.

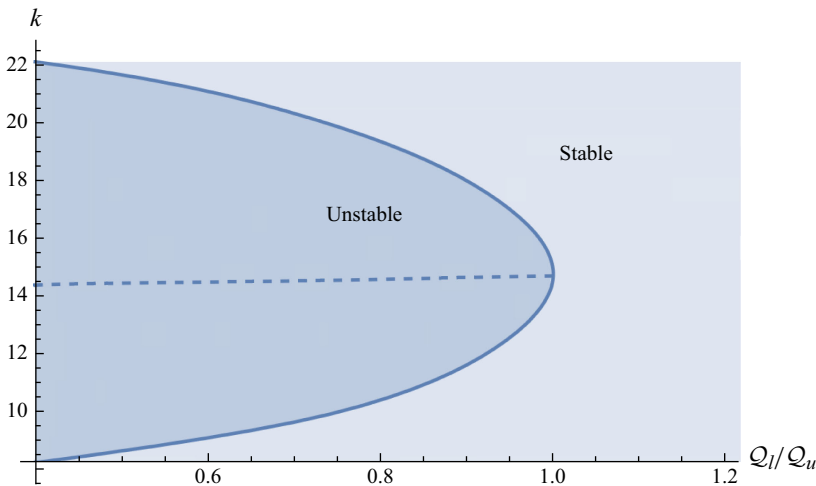


Figure 9. Neutral stability curve (solid) displaying the neutral flux ratio  $Q_l/Q_u$  as a function of the wavenumber, also showing the critical wavenumber  $k_c$  (dashed), when  $\mathcal{D} = 0.1$ ,  $\mathcal{M} = 120$  and  $Q_l + Q_u = 1$ . The flow is unstable for flux ratios above this neutral stability curve.

We find that the instability is suppressed completely for a sufficiently small total flux  $Q_l + Q_u$  and sufficiently large flux ratio  $Q_l/Q_u$ , as depicted in figures 8 and 9. The interval of unstable wavenumbers expands as the total source flux increases and the flux ratio decreases. The critical wavenumber increases with the total source flux and remains approximately constant with respect to the flux ratio. We can therefore expect to see an increasing number of fingers when the total source flux increases, which is consistent with recent experiments in which the intruding fluid is supplied from below (Kumar *et al.* 2021).

We condense information further in a contour plot of the maximal growth rate  $\sigma_{max}$  versus the total flux and flux ratio, shown in figure 10. As seen in figure 10, growth rates are largest when the total flux is large and a sufficiently large total flux (of order unity) is required for the onset of instability. Equivalently, the onset of instability requires the flux

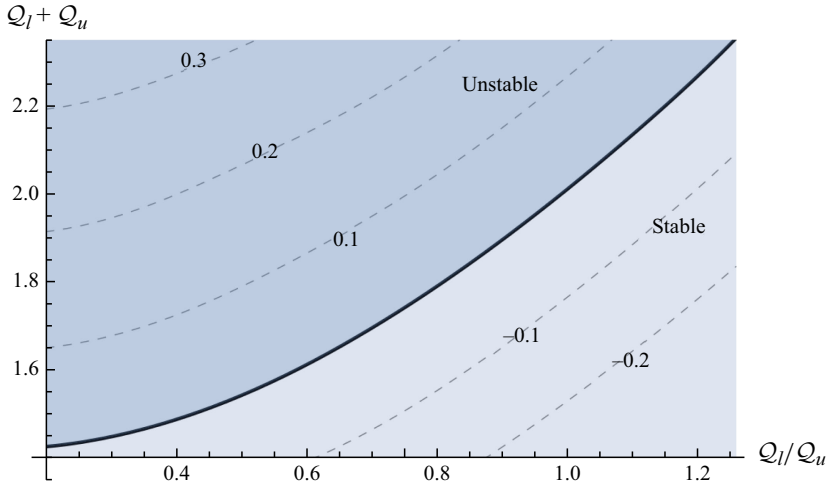


Figure 10. Contour plot of the maximal growth rate  $\sigma_{max}$  versus the flux ratio  $Q_l/Q_u$  and total flux  $Q_l + Q_u$ , with the neutral stability curve ( $\sigma_{max} = 0$ ) displayed as a thick solid curve. The remaining parameter values are  $\mathcal{M} = 120$  and  $\mathcal{D} = 0.1$ . The flow is unstable when the total flux is large and flux ratio is small.

of the upper layer to be sufficiently large relative to that of the lower layer. This is in line with the experiments of Lister & Kerr (1989), in which a low-viscosity fluid intrudes at the interface between two other fluids and no instabilities were observed, save for small-scale frontal patterning that the authors attribute to contamination of the fluid surface by dust. These experiments were carried out for dimensionless fluxes in the range  $8.7 \times 10^{-6}$ – $5.3 \times 10^{-5}$ , which is much less than the threshold (of order unity) required for instability. The threshold is also consistent with the experiments of Dauck (2020), for which the dimensionless flux reached up to approximately 160 and instabilities were observed.

The stability thresholds discussed in this section are summarised in the most condensed contour plot shown in figure 11, displaying the critical total flux required for the onset of instability in  $(\mathcal{D}, \mathcal{M})$  space for various values of the flux ratio. Values of the critical viscosity ratio and critical density difference required for the onset of instability can be read off from figure 11. Alternatively, figure 11 can be interpreted as a plot of the critical viscosity ratio versus the density difference for various values of the total flux and flux ratio. The higher the total flux, the lower the viscosity ratio required for the onset of instability, and the larger the interval of density differences for which instabilities appear.

#### 4.2. Mechanism of instability and suppression

To understand the mechanism of instability physically, it is instructive to compare with classical viscous fingering in porous-media/Hele-Shaw cells. The mechanisms of instability are similar in that there is less flow resistance along the fingers of a less viscous fluid than in the gaps between them filled with a more viscous fluid, thus resulting in the fingers growing (when the intruding fluid is less viscous than the ambient). However, in the free-surface case examined here, the intruding fluid is also advancing into atmosphere (which is less viscous, so the viscosity contrast is stabilising), so finger growth is reliant on the intruding fingers displacing the lubricating liquid ‘more’ than displacing the atmosphere. In other words, finger growth requires the density difference  $\mathcal{D}$  to be sufficiently small (as seen in figure 6) and the upper-layer flux  $Q_u$  to be sufficiently large relative to the lower-layer flux  $Q_l$  and relative to unity (as seen in figures 8–10) that the fingers can sink down into rather than just riding on top of the lubricating layer.

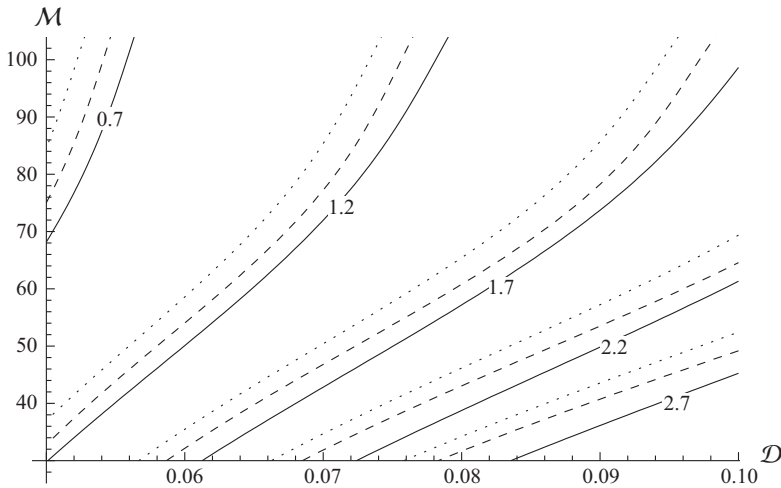


Figure 11. Contour plot of the critical total flux  $Q_l + Q_u$  required for the onset of instability in  $(D, M)$  space when  $Q_l/Q_u = 0.4$  (solid curves),  $0.5$  (dashed curves) and  $0.6$  (dotted curves).

In contrast, when the less viscous fluid intrudes beneath another thin film of viscous fluid (the set-up of Kowal & Worster 2019a,b), it is not stabilised by its advance into a less viscous atmosphere and so the instability thresholds are lower than reported here. In particular, the critical viscosity ratio required for the onset of instability in the set-up of Kowal & Worster (2019a,b) is of order unity when the intruding layer is supplied from below, which is one to two orders of magnitude smaller than when the less viscous fluid intrudes from above as in the current work. However, the general trends in the stability thresholds are qualitatively similar as the parameters vary. For example, for both systems, there is a critical density difference above which the instabilities are compressed, with the interval of unstable wavenumbers widening as the density difference decreases. The critical density difference is of order unity (versus one tenth) when the less viscous fluid intrudes from below (versus above).

To explore the mechanism of suppression further, it is also instructive to focus on contributions that are significant for large density differences. Non-zero density differences between the two layers of viscous fluid give rise to additional buoyancy forces within the lower layer near the front of the intruding fluid. These are associated with the gravitational spreading of the underlying layer under its own weight, dragging the upper layer along with it. As gradients of the lower-layer thickness are positive near the front when the density difference is non-zero, the contributions to the flow velocity, arising from the spreading of the lower layer under its own weight, are negative within the underlying layer. This, in turn, induces an inwards contribution to the flow, seen most clearly in the velocity profiles of figure 5 of Yang *et al.* (2024). That is, in what would have been an unstable configuration, this contribution involves a more viscous fluid intruding (inwards) into a less viscous fluid, which is stabilising.

Similar buoyancy forces stabilise the flow of single-layer viscous gravity currents, where a viscous fluid intrudes into air (less viscous) – a stable viscosity contrast (Mathunjwa & Hogg 2006). Small perturbations to single-layer viscous gravity currents, which are driven by buoyancy forces alone, have been found to decay and the flow has been found to approach a similarity solution at late times (Mathunjwa & Hogg 2006; Ball & Huppert 2019). For two-layer flows, these buoyancy forces contribute to the flow only when the densities of the two viscous fluids are unequal. When the density difference increases,

so does the effect of these buoyancy forces, especially near the front, where they are most profound as depicted in [figure 5](#) of Yang *et al.* (2024). As the instability is a frontal instability, the dynamics near the front, and particularly the effect of these buoyancy forces, is what determines the onset of instability, and hence it is natural to expect these forces to have a stabilising effect when the density difference is sufficiently large, as seen in [figure 6](#).

## 5. Conclusions

In this work, we have demonstrated that a free-surface flow consisting of a thin film of viscous fluid intruding over another layer of fluid of dissimilar viscosity and density is prone to a new type fingering instability, termed the non-porous viscous fingering instability. This type of instability is most closely related to Saffman–Taylor viscous fingering in a porous medium or a Hele–Shaw cell, but this time without a porous medium or Hele–Shaw cell present. The similarity between these two types of instability is that a viscosity contrast between two fluids is needed for both instabilities to occur. The difference between them is that the jump in pressure gradient driving the instabilities is hydrostatic for the former and dynamic for the latter form of instability.

We also point out features distinguishing the non-porous viscous fingering instability from other frontal instabilities, including the fingering of a driven spreading film and thermoviscous fingering. We found that a free-surface flow of a low-viscosity fluid is more prone to instability when intruding into a high-viscosity fluid from below (as in Kowal & Worster 2019*a,b*) than from above (as in the present paper). Intuitively, this is because the less viscous fluid also displaces the atmosphere (an even less viscous fluid) in the latter scenario, which is stabilising.

We have also examined the stabilising influence of buoyancy forces, which form near the nose of a thin film of viscous fluid as it intrudes into another viscous fluid of different density and viscosity. These buoyancy forces are greatest near the front of the intruding layer and feature as the only physical mechanism driving the flow of single-layer viscous gravity currents, for example. Such buoyancy forces have been shown to be stabilising for single-layer flows (Grundy & McLaughlin 1982; Mathunjwa & Hogg 2006) and for two-phase flows, when the intruding layer is supplied from below (Kowal & Worster 2019*a,b*) or when it completely displaces the ambient layer (Kowal 2021).

We found that a sufficiently large viscosity ratio is required in order for the instability to occur, and that the instability is suppressed completely for large enough density differences between the two layers. For large enough density differences, driving buoyancy forces associated with the gravitational spreading of the lubricating layer under its own weight become more pronounced, and stabilise the flow completely. For lower density differences, for which the system is unstable, this mechanism provides for wavelength selection, stabilising the flow for large wavenumbers in contrast to intermediate wavenumbers. This indicates that the hydrodynamic interactions of the two layers of viscous fluid alone suffice in stabilising the flow for large wavenumbers, giving rise to wavelength selection. This contrasts with classical Saffman–Taylor viscous fingering, which is instead stabilised by other mechanisms, such as the effects of surface tension or fluid mixing, for example. Such effects, however, may further stabilise the flow considered in this work, likely leading to smaller growth rates for large wavenumbers and smaller critical wavenumbers.

We also found evidence of the role of the source flux in the onset of these fingering instabilities. In particular, the flow is unstable only when the source flux of the upper layer is large enough relative to that of the lower layer, which is consistent with available experimental observations when the intruding fluid is supplied from below, for various rheologies, and from above.

Our observations may shed light on the appearance and possible suppression mechanisms of similar fingering instabilities found in nature and industry at various length and time scales, modulo the influence of secondary effects such as surface tension, or fluid mixing, for instance. Examples include drug-mucus interactions in nasal drug/vaccine delivery, the manufacture of patterned substrates and the interaction of dissimilar lava flows, for example.

**Acknowledgements.** We would like to thank N.J. Mottram for insightful discussions.

**Funding.** H.Y. acknowledges the support of an EPSRC studentship. K.N.K. acknowledges the support of EPSRC grant EP/Y021959/1.

**Declaration of interests.** The authors report no conflict of interest.

**Data availability statement.** The data that support the findings of this study are directly available within this publication.

## Appendix A. Asymptotic expansions near the intrusion front

Similar to the base flows of Yang *et al.* (2024), we find that the thicknesses of the two layers can be expanded as

$$\begin{aligned} F(\xi, \vartheta, \tau) &\sim A_1(\vartheta, \tau)\delta^{\frac{1}{2}} + A_2(\vartheta, \tau)\delta + A_3(\vartheta, \tau)\delta^{\frac{3}{2}} \dots, \\ f(\xi, \vartheta, \tau) &\sim a_0(\vartheta, \tau) + a_1(\vartheta, \tau)\delta^{\frac{1}{2}} + a_2(\vartheta, \tau)\delta + a_3(\vartheta, \tau)\delta^{\frac{3}{2}} \dots \end{aligned} \quad (\text{A1})$$

near the intrusion front where  $\delta = (1 - \xi/\xi_N) \ll 1$ .

For the governing equation (3.7) describing the lower layer, the leading-order contribution is of  $O(\delta^{-3/2})$  and yields the relationship

$$(\mathcal{D} + 1)a_1 + A_1 = 0 \quad (\text{A2})$$

between  $A_1$  and  $a_1$ . The leading-order contribution of the governing equation (3.6) for the upper layer is of  $O(\delta^{-1/2})$  and gives rise to

$$(\mathcal{D} + 1)a_2 + A_2 + \frac{A_1^2 \mathcal{D}}{a_0(\mathcal{D} + 1)} - \frac{\xi_N^2}{3a_0^2} - \frac{2\xi_N}{3a_0^2} \frac{\partial \xi_N}{\partial \tau} + O\left(\frac{\partial}{\partial \vartheta} \times \frac{\partial}{\partial \vartheta}\right) = 0, \quad (\text{A3})$$

where  $O((\partial/\partial \vartheta) \times (\partial/\partial \vartheta))$  represent terms that contain products of two azimuthal derivatives, which are zero for the base solution and negligible for small-amplitude perturbations. This equation is identical to the equivalent equation for the base flow apart from the addition of the term containing a derivative with respect to  $\tau$  and the (negligible) higher-order terms.

Going to the next order, the  $O(\delta^{-1/2})$  contribution to (3.7) and the  $O(1)$  contribution to (3.6) yield

$$(\mathcal{D} + 1)a_3 + A_3 + \gamma_1 + O\left(\frac{\partial}{\partial \vartheta} \times \frac{\partial}{\partial \vartheta}\right) = 0, \quad (\text{A4})$$

$$(\mathcal{D} + 1)a_3 + A_3 + \gamma_2 + O\left(\frac{\partial}{\partial \vartheta} \times \frac{\partial}{\partial \vartheta}\right) = 0, \quad (\text{A5})$$

respectively, where

$$\gamma_1 = -\frac{A_1^3 \mathcal{D}}{a_0^2(\mathcal{D} + 1)^2} - \frac{A_2 A_1 (2 - 3\mathcal{D})}{2a_0(\mathcal{D} + 1)} + \frac{A_1 \xi_N^2}{3a_0^3(\mathcal{D} + 1)} - \frac{a_2 A_1}{a_0} + \frac{2A_1 \xi_N}{3a_0^3(1 + \mathcal{D})} \frac{\partial \xi_N}{\partial \tau}, \quad (\text{A6})$$

and

$$\gamma_2 = \frac{2A_1^3 \mathcal{D}(\mathcal{D}\mathcal{M} + \mathcal{M} - 3)}{9a_0^2(\mathcal{D} + 1)^2} + \frac{8A_2A_1\mathcal{D}}{3a_0(\mathcal{D} + 1)} + \frac{2a_2A_2(\mathcal{D} + 1)}{3A_1} - \frac{2A_2\xi_N^2}{9a_0^2A_1} + \frac{2A_2^2}{3A_1} - \frac{4A_2\xi_N}{9a_0^2A_1} \frac{\partial \xi_N}{\partial \tau}. \quad (\text{A7})$$

Similarly to before, these coefficients generalise those describing the base flow through the addition of terms involving derivatives with respect to  $\tau$  and the higher-order terms. We note that (A4) and (A5) depend on  $A_3$  and  $a_3$  through the combination  $(\mathcal{D} + 1)a_3 + A_3$ , which can be eliminated by subtracting (A4) from (A5), which gives

$$\gamma_1 = \gamma_2. \quad (\text{A8})$$

Finally, solving (A3) and (A8) for  $A_2$  and  $a_2$  yields

$$A_2 = -\frac{4A_1^2}{9a_0} \left( \mathcal{M} - \frac{3}{\mathcal{D} + 1} \right), \quad (\text{A9})$$

$$a_2 = \frac{1}{9(\mathcal{D} + 1)a_0^2} \left[ 3\xi_N \left( \xi_N + 2\frac{\partial \xi_N}{\partial \tau} \right) + A_1^2 a_0 \left( 4\mathcal{M} - 9 - \frac{3}{\mathcal{D} + 1} \right) \right], \quad (\text{A10})$$

specifying  $a_2$  and  $A_2$  in terms of  $a_0$ ,  $A_1$  and  $\xi_N$ .

## Appendix B. Perturbed fluxes

Explicit expressions for perturbations to the fluxes are given by (3.27)–(3.30), where

$$\alpha_{u1} = -\frac{3}{\xi_{N0}} F_0 \left[ f_0 ((\mathcal{D} + 1)f'_0 + F'_0) + F_0 (f'_0 + F'_0) \right], \quad (\text{B1})$$

$$\alpha_{u2} = -\frac{3}{2\xi_{N0}} \left[ f_0^2 ((\mathcal{D} + 1)f'_0 + F'_0) + 2\mathcal{M}F_0^2 (f'_0 + F'_0) + 4f_0F_0 (f'_0 + F'_0) \right], \quad (\text{B2})$$

$$\alpha_{u3} = -\frac{1}{2\xi_{N0}} F_0 \left[ 3(\mathcal{D} + 1)f_0^2 + 6f_0F_0 + 2\mathcal{M}F_0^2 \right], \quad (\text{B3})$$

$$\alpha_{u4} = -\frac{1}{2\xi_{N0}} F_0 \left[ 6f_0F_0 + 3f_0^2 + 2\mathcal{M}F_0^2 \right], \quad (\text{B4})$$

$$\alpha_{u5} = \frac{1}{2\xi_{N0}^2} F_0 \left[ 3f_0^2 ((\mathcal{D} + 1)f'_0 + F'_0) + 2\mathcal{M}F_0^2 (f'_0 + F'_0) + 6f_0F_0 (f'_0 + F'_0) \right], \quad (\text{B5})$$

$$\alpha_{l1} = -\frac{3}{\xi_{N0}} f_0 \left[ ((\mathcal{D} + 1)f_0 + F_0) f'_0 + (f_0 + F_0) F'_0 \right], \quad (\text{B6})$$

$$\alpha_{l2} = -\frac{3}{2\xi_{N0}} f_0^2 (f'_0 + F'_0), \quad (\text{B7})$$

$$\alpha_{l3} = -\frac{1}{2\xi_{N0}} f_0^2 (2(\mathcal{D} + 1)f_0 + 3F_0), \quad (\text{B8})$$

$$\alpha_{l4} = -\frac{1}{2\xi_{N0}} f_0^2 (2f_0 + 3F_0), \quad (\text{B9})$$

$$\alpha_{l5} = \frac{1}{2\xi_{N0}^2} f_0^2 \left[ 2f_0 ((\mathcal{D} + 1)f'_0 + F'_0) + 3F_0 (f'_0 + F'_0) \right]. \quad (\text{B10})$$



REFERENCES

- AL-HOUSSEINY, T.T., TSAI, P.A. & STONE, H.A. 2012 Control of interfacial instabilities using flow geometry. *Nat. Phys.* **8** (10), 747–750.
- ALGWAISH, G. & NAIRE, S. 2023 The thermo-viscous fingering instability of a cooling spreading liquid dome. *Phys. Fluids* **35** (11), 112109.
- BALL, T.V. & HUPPERT, H.E. 2019 Similarity solutions and viscous gravity current adjustment times. *J. Fluid Mech.* **874**, 285–298.
- BALMFORTH, N.J. & CRASTER, R.V. 2000 Dynamics of cooling domes of viscoplastic fluid. *J. Fluid Mech.* **422**, 225–248.
- BEN-JACOB, E. 1997 From snowflake formation to growth of bacterial colonies II: Cooperative formation of complex colonial patterns. *Contemp. Phys.* **38** (3), 205–241.
- BEN-JACOB, E., SCHMUELI, H., SHOCHET, O. & TENENBAUM, A. 1992 Adaptive self- organisation during growth of bacterial colonies. *Physica A* **187** (3–4), 378–424.
- BISCHOFBERGER, I., RAMACHANDRAN, R. & NAGEL, S.R. 2014 Fingering versus stability in the limit of zero interfacial tension. *Nat. Commun.* **5** (1), 5265.
- CHRISTY, I. & HINTON, E.M. 2023 Two-layer gravity currents of generalized Newtonian fluids. *Proc. R. Soc. A* **479** (2279), 2279.
- CINAR, Y., RIAZ, A. & TCHELEPI, H.A. 2009 Experimental study of CO<sub>2</sub> injection into saline formations. *Soc. Petrol. Engrs J.* **14** (04), 589–594.
- DAUCK, T.-F. 2020 Viscous fingering instabilities and gravity currents, *PhD thesis*, University of Cambridge, UK.
- DAUCK, T.-F., BOX, F., GELL, L., NEUFELD, J.A. & LISTER, J.R. 2019 Shock formation in two-layer equal-density viscous gravity currents. *J. Fluid Mech.* **863**, 730–756.
- DIAS, E.O. & MIRANDA, J.A. 2010 Control of radial fingering patterns: a weakly nonlinear approach. *Phys. Rev. E* **81** (1), 016312.
- FAST, P., KONDIC, L., SHELLEY, M.J. & PALFFY-MUHORAY, P. 2001 Pattern formation in non-Newtonian Hele–Shaw flow. *Phys. Fluids* **13** (5), 1191–1212.
- FINK, J.H. & GRIFFITHS, R.W. 1990 Radial spreading of viscous-gravity currents with solidifying crust. *J. Fluid Mech.* **221**, 485–509.
- FINK, J.H. & GRIFFITHS, R.W. 1998 Morphology, eruption rates and rheology of lava domes: insights from laboratory models. *J. Geophys. Res.* **103** (B1), 527–545.
- GRUNDY, R.E. & MCLAUGHLIN, R. 1982 Eigenvalues of the Barenblatt–Pattle similarity solution in nonlinear diffusion. *Proc. R. Soc. Lond. A* **383** (1784), 89–100.
- GYLLENBERG, A.A. & SAYAG, R. 2022 Lubricated axisymmetric gravity currents of power-law fluids. *J. Fluid Mech.* **949**, A40.
- HEWITT, I.J. 2013 Seasonal changes in ice sheet motion due to melt water lubrication. *Earth Planet. Sci. Lett.* **371–372**, 16–25.
- HINDMARSH, R.C.A. 2004 Thermoviscous stability of ice-sheet flows. *J. Fluid Mech.* **502**, 17–40.
- HINDMARSH, R.C.A. 2009 Consistent generation of ice-streams via thermo-viscous instabilities modulated by membrane stresses. *Geophys. Res. Lett.* **36**, L06502.
- HINTON, E.M. 2022 Inferring rheology from free-surface observations. *J. Fluid Mech.* **937**, 2202–02893.
- HOMSY, G.M. 1987 Viscous fingering in porous media. *Annu. Rev. Fluid Mech.* **19** (1), 271–311.
- HULL, D. 1999 *Fractology*. Cambridge University Press.
- HUPPERT, H.E. 1982a Flow and instability of a viscous current down a slope. *Nature* **300** (5891), 427–429.
- HUPPERT, H.E. 1982b The propagation of two-dimensional and axisymmetric viscous gravity currents over a rigid horizontal surface. *J. Fluid Mech.* **121**, 43–58.
- JUEL, A. 2012 Flattened fingers. *Nat. Phys.* **8** (10), 706–707.
- KONDIC, L., SHELLEY, M.J. & PALFFY-MUHORAY, P. 1998 Non-Newtonian Hele–Shaw flow and the Saffman–Taylor instability. *Phys. Rev. Lett.* **80** (7), 1433–1436.
- KOWAL, K.N. 2021 Viscous banding instabilities: non-porous viscous fingering. *J. Fluid Mech.* **926**, A4.
- KOWAL, K.N. & WORSTER, M.G. 2019a Stability of lubricated viscous gravity currents. Part 1. Internal and frontal analyses and stabilisation by horizontal shear. *J. Fluid Mech.* **871**, 970–1006.
- KOWAL, K.N. & WORSTER, M.G. 2019b Stability of lubricated viscous gravity currents. Part 2. Global analysis and stabilisation by buoyancy forces. *J. Fluid Mech.* **871**, 1007–1027.
- KOWAL, K.N. & WORSTER, M.G. 2015 Lubricated viscous gravity currents. *J. Fluid Mech.* **766**, 626–655.
- KUMAR, P., ZURI, S., KOGAN, D., GOTTLIEB, M. & SAYAG, R. 2021 Lubricated gravity currents of power-law fluids. *J. Fluid Mech.* **916**, A33.
- LEUNG, L.T. & KOWAL, K.N. 2022a Lubricated viscous gravity currents of power-law fluids. Part 1. Self-similar flow regimes. *J. Fluid Mech.* **940**, A26.

- LEUNG, L.T. & KOWAL, K.N. 2022*b* Lubricated viscous gravity currents of power-law fluids. Part 2. Stability analysis. *J. Fluid Mech.* **940**, A27.
- LI, S., LOWENGRUB, J.S., FONTANA, J. & PALFFY-MUHORAY, P. 2009 Control of viscous fingering patterns in a radial Hele–Shaw cell. *Phys. Rev. Lett.* **102** (17), 174501.
- LISTER, J.R. & KERR, R.C. 1989 The propagation of two-dimensional and axisymmetric viscous gravity currents at a fluid interface. *J. Fluid Mech.* **203**, 215–249.
- LUO, R.I., CHEN, Y. & LEE, S. 2018 Particle-induced viscous fingering: Review and outlook. *Phys. Rev. Fluids* **3** (11), 110502.
- MASIUK, T., KADAKIA, P. & WANG, Z. 2016 Development of a physiologically relevant dripping analytical method using simulated nasal mucus for nasal spray formulation analysis. *J. Pharmaceut. Anal.* **6** (5), 283–291.
- MATHUNJWA, J.S. & HOGG, A.J. 2006 Self-similar gravity currents in porous media: linear stability of the Barenblatt–Pattle solution revisited. *Eur. J. Mech. B-Fluids* **25** (3), 360–378.
- MORROW, L.C., MORONEY, T.J. & MCCUE, S.W. 2019 Numerical investigation of controlling interfacial instabilities in non-standard Hele–Shaw configurations. *J. Fluid Mech.* **877**, 1063–1097.
- MULLINS, W.W. & SEKERKA, R.F. 1964 Stability of a planar interface during solidification of a dilute binary alloy. *J. Appl. Phys.* **35** (2), 444–451.
- NASE, J., DERKS, D. & LINDNER, A. 2011 Dynamic evolution of fingering patterns in a lifted Hele–Shaw cell. *Phys. Fluids* **23** (12), 123101.
- ORR, F.M. & TABER, J.J. 1984 Use of carbon dioxide in enhanced oil recovery. *Science* **224** (4649), 563–569.
- PERKINS, T.K., JOHNSTON, O.C. & HOFFMAN, R.N. 1965 Mechanics of viscous fingering in miscible systems. *Soc. Petrol. Engrs J.* **5** (04), 301–317.
- PIHLER-PUZOVIC, D., ILLIEN, P., HEIL, M. & JUEL, A. 2012 Suppression of complex fingerlike patterns at the interface between air and a viscous fluid by elastic membranes. *Phys. Rev. Lett.* **108** (7), 074502.
- PIHLER-PUZOVIC, D., PERILLAT, R., RUSSELL, M., JUEL, A. & HEIL, M. 2013 Modelling the suppression of viscous fingering in elastic-walled Hele–Shaw cells. *J. Fluids Mech.* **731**, 161–183.
- SAFFMAN, P.G. & TAYLOR, G. 1958 The penetration of a fluid into a porous medium or Hele–Shaw cell containing a more viscous liquid. *Proc. R. Soc. Lond. A* **245** (1242), 312–329.
- SHAH, K.S., PEGLER, S.S. & MINCHEW, B.M. 2021 Two-layer fluid flows on inclined surfaces. *J. Fluid Mech.* **917**, A54.
- SMITH, S.H. 1969 On initial value problems for the flow in a thin sheet of viscous liquid. *J. Appl. Maths Phys.* **20** (4), 556–560.
- TAYLOR, G.I. 1963 Cavitation of a viscous fluid in narrow passages. *J. Fluid Mech.* **16** (4), 595–619.
- TROIAN, S.M., HERBOLZHEIMER, E., SAFRAN, S.A. & JOANN, J.F. 1989 Fingering instabilities of driven spreading films. *Europhys. Lett.* **10** (1), 25–30.
- VAQUERO-STAINER, C., HEIL, M., JUEL, A. & PIHLER-PUZOVIĆ, D. 2019 Self-similar and disordered front propagation in a radial Hele–Shaw channel with time-varying cell depth. *Phys. Rev. Fluids* **4** (6), 064002.
- YAN, Z. & KOWAL, K.N. 2024 A controllable sliding law for thin-film flows over slippery fluid-saturated substrates: theory and experiments. *J. Fluid Mech.* **982**, A14.
- YANG, H., MOTTRAM, N.J. & KOWAL, K.N. 2024 Dynamics of a thin film of fluid spreading over a lubricated substrate. *J. Fluid Mech.* **1001**, A47.
- ZHENG, Z., KIM, H. & STONE, H.A. 2015 Controlling viscous fingering using time-dependent strategies. *Phys. Rev. Lett.* **115** (17), 174501.